Atomic-level simulations of epitaxial recrystallization and amorphous-to-crystalline transition in 4*H*-SiC

F. Gao,[1,*] Y. Zhang,[1] M. Posselt,[2] and W. J. Weber[1]
[1]*Pacific Northwest National Laboratory, MS K8-93, P. O. Box 999, Richland, Washington 99354, USA*
[2]*Forschungszentrum Rossendorf, Institute of Ion Beam Physics and Materials Research, P. O. Box 510119, D-01314 Dresden, Germany*

(Received 8 February 2006; revised manuscript received 1 June 2006; published 14 September 2006)

The amorphous-to-crystalline transition in 4*H*-SiC has been studied using molecular dynamics (MD) methods, with simulation times of up to a few hundred ns and at temperatures ranging from 1000 to 2000 K. Two nanosized amorphous layers, one with the normal of the *a*-*c* interfaces along the $[\bar{1}2\bar{1}0]$ direction and the other along the $[\bar{1}010]$ direction, were created within a crystalline cell to study epitaxial recrystallization and the formation of secondary phases. The recovery of bond defects at the interfaces is an important process driving the epitaxial recrystallization of the amorphous layers. The amorphous layer with the *a*-*c* interface normal along the $[\bar{1}2\bar{1}0]$ direction can be completely recrystallized at temperatures of 1500 and 2000 K, but the recrystallized region is defected with dislocations and stacking faults. On the other hand, the recrystallization process for the *a*-*c* interface normal along the $[\bar{1}010]$ direction is hindered by the nucleation of polycrystalline phases, and these secondary phases are stable for longer simulation times. A general method to calculate activation energy spectra is employed to analyze the MD annealing simulations, and the recrystallization mechanism in SiC consists of multiple stages with activation energies ranging from 0.8 to 1.7 eV.

DOI: 10.1103/PhysRevB.74.104108 PACS number(s): 61.72.Cc, 61.43.Dq, 61.82.Fk, 81.40.Ef

I. INTRODUCTION

The importance of silicon carbide (SiC) has been emphasized for a wide range of technological applications, such as optoelectronic devices and high temperature electronics,[1] as well as structure components in nuclear reactors,[2,3] because of its excellent chemical stability, good electronic properties, high stiffness, and high hardness. One exciting application of SiC could be in deep-space missions, where nuclear power is needed for the craft. Radiation-resistant silicon carbide devices would reduce the shielding demanded to protect reactor control electronics. For industrial scale SiC-device fabrication, ion implantation is a major technique for electrical dopant incorporation, since conventional diffusion-based techniques cannot be applied due to the very low diffusivity of dopants.[4,5] However, the interactions of high energetic ions or neutrons with SiC inevitably produce defects, defect clusters and disordering. In particular, high dose ion implantation for *p*-type doping, which is necessary to achieve comparable electrical conductivity as compared with Si semiconductors, would lead to amorphization due to damage accumulation at room temperature. Consequently, a number of experimental and theoretical studies have been devoted to understanding defect production,[6,7] defect accumulation and amorphization,[8,9] and amorphization kinetics.[10] Thermal annealing at high temperature is generally required for damage recovery and epitaxial recrystallization. Understanding the kinetics and mechanisms of recrystallization has been identified as a key issue in the development of next-generation semiconductor devices.

It is generally accepted that ion-beam-amorphized SiC is very stable against thermal annealing, and temperatures higher than 1723 K are necessary for its recrystallization.[11] Such extremely high temperatures are not suitable for most technology processes. The annealing behavior has been studied by Rutherford backscattering spectroscopy (RBS),[12,13] which determines the relative lattice disorder, and by transmission electron microscopy,[14] in which amorphous layers were observed to recrystallize. Ion-beam-induced epitaxial crystallization has been observed to occur at a temperature as low as 735 K;[15] however, the quality of the recrystallized SiC layer is poor due to the accumulation of irradiation defects and the formation of growth defects.

In order to obtain insights into the dynamic processes of ordering and the pathways to recrystallization, atomic-level simulations are needed to explore the mechanisms controlling the amorphous-to-crystalline (*a*-*c*) transition and the nucleation and growth of polycrystalline secondary phases. Previously, several atomic simulations have been applied to study solid-phase epitaxial growth (SPEG) in Si (Ref. 16) and Ge,[17] dealing with recrystallization of amorphous materials. Starting with crystalline nuclei of different size embedded in an amorphous matrix, the evolution of the system at the atomic level was followed. The most important model of recrystallization at a planar *a*-*c* interface in Si has been developed by Spaepen and Turnbull,[18] which predicts that recrystallization should occur at the interface due to bond breaking and migration of dangling bonds that reconstruct the random network into the crystalline network. However, the detail analysis of one simple and one complex microscopic mechanism during atomic-level simulations of SPEG in Si (Ref. 19) has cast doubt on the common viewpoint of an unique activation energy, as proposed by Spaepen and Turnbull.[18] MD simulations have been previously employed to study epitaxial recrystallization, nucleation and growth of secondary ordered phases, and phase transformation in 3*C*-SiC.[20,21] The results have shown that the recrystallization mechanism in SiC consists of multiple stages, and a general method of analysis is employed to obtain an activation energy spectrum that ranges from about 0.8 to 2.3 eV.

In the present work, two nanosized amorphous layers, one with the normal of the *a*-*c* interfaces along the $[\bar{1}2\bar{1}0]$ direction and another along the $[\bar{1}010]$ direction, in 4*H*-SiC are studied. These two directions were chosen for the present studies because it has been reported that the $(\bar{1}2\bar{1}0)$-oriented SiC shows significantly higher channel mobility than that for (0001) SiC.[22] The investigation of the annealing behavior of the implanted amorphous layer in $(\bar{1}2\bar{1}0)$- and $(\bar{1}010)$-oriented SiC is important for the fabrication of electronic devices based on these orientations. Furthermore, both the $[\bar{1}2\bar{1}0]$ and $[\bar{1}010]$ directions are in the basal plane, but they have different atomic stacking sequences, such that a full comparison of annealing process can be made. The annealing simulations of the amorphous zones are performed using MD methods, with the aim of developing a microscopy understanding of recrystallization mechanisms in 4*H*-SiC. A number of features in the epitaxial recrystallization, including the nucleation and subsequent growth of secondary phases, as well as the mechanisms controlling the evolution of these processes, are reported. Furthermore, the simulation results are discussed and compared with available experimental observations and with simulation results of SPEG in 3*C*-SiC.

II. COMPUTATIONAL METHOD

The series of MD simulations reported here were done using a modified version of the MOLDY computer code, with a variable time step algorithm and a Brenner-type empirical potential[23] that is combined with Ziegler-Biersack-Littmark potential[24] at separation distance less than 0.1 nm. Defect formation energies and stable configurations predicted by this parametrized potential are in good agreement with those calculated by density functional theory,[23] and the activation energies for spontaneous recovery of Frenkel pairs are quantitatively consistent with the recovery processes observed experimentally below room temperature.[25] In a recent *ab initio* study of interstitial and vacancy recombination, Bockstedte *et al.*[26] found that the activation energies calculated using the Brenner-type potential are generally in agreement with their results for neutral Frenkel-pairs. However, it should be noted that some interstitial configurations (i.e., the tetrahedral Si-coordinated *C* interstitial calculated using this potential) are unstable in the *ab initio* calculations[26] and spontaneously convert to *C*-*C* split interstitials. These differences should have a small effect on the present simulations because the recombination activation energies of these tetrahedral Si-coordinated interstitials are similar to those of *C*-*C* split interstitials. Furthermore, the migration energies of native point defects determined using this potential are in agreement with *ab initio* data and experimental results.[27] These results suggest that the model potential should be well suited for recrystallization studies in SiC. Another important issue is that the defects in SiC may be charged, and the migration paths and activation barriers strongly depend on their charged state, as demonstrated by recent *ab initio* calculations.[26,28] Since the annealing simulations are carried out at high temperatures, where the Fermi level effect is not pronounced, the relevant interstitials and Frenkel pairs are in neutral charge states. Therefore, the present MD simulation with the model potential should provide a reasonable approach for simulation studies of recrystallization in SiC.

Two amorphous configurations were produced for the current studies. These models have rectangular simulation cells that extend along the $[\bar{1}2\bar{1}0]$ direction (denoted as M_x) or the $[\bar{1}010]$ direction (M_y). The simulation cells consisted of $40a_0 \times 2a_0 \times 6a_0$ and $3a_0 \times 40a_0 \times 4a_0$ unit cells, with 7680 movable atoms for the models M_x and M_y, respectively. Periodic boundary conditions were applied to all three directions. To generate a nanosized amorphous zone in both models, the MD block was divided along the longitudinal axis into 40 layers, and each layer contains 192 atoms in a perfect crystal of 4*H*-SiC. A Gaussian-profile heat spike was initiated by applying a suitable distribution of kinetic energy to the atoms of the central 20 layers, with a maximum temperature of 6000 K. Similar to previous studies,[21] the crystal was equilibrated for 0.2 ns to allow fully mixing in the central region of the crystal, and then quenched to 0 K at the rate of 10^{13} K/s. The system was relaxed for another 50 ps under zero-external pressure conditions, and rescaled to a specific annealing temperature, which ranged from 1000 to 2000 K. The annealing simulations were carried out under constant pressure and temperature conditions, and simulation times were extended to 260 ns.

III. ANNEALING THE M_x MODEL

The amorphous structure at the center of a crystal extended along $[\bar{1}2\bar{1}0]$ is shown in Fig. 1(a), where gray spheres represent C atoms and dark spheres indicate Si atoms. It can be seen that the central part of the crystal lacks any degree of periodicity, with no evidence of long-range order. Two interfaces are created between the amorphous phase and the crystalline host phase. An analysis of the pair-correlation function, bond angles, and bond length indicates that the central disordered region is a liquidlike structure that is consistent with an amorphous state. The partial pair-correlation functions shown in Fig. 1(b) demonstrate that the first nearest neighbor is centered at 0.188 nm for SiC pairs, and the second nearest neighbors are centered 0.304 and 0.308 nm for Si-Si and C-C pairs, respectively. These peaks correspond to the short-range order in crystalline SiC. However, C-C and Si-Si homonuclear bond peaks are visible at about 0.165 and 0.252 nm, respectively. These subpeak positions are consistent with observed bond peaks at about 0.15 and 0.24 nm in 6*H*-SiC amorphized by electrons[8] and ions,[29,30] implying the existence of sp^2- and sp^3-bonded carbon atoms in the amorphous SiC (*a*-SiC).

Although long-range order does not exist in the *a*-SiC, partial short-range order is still retained. The extent of short-range disorder can be quantified by the fraction of homonuclear bonds.[30,31] Because of the difficulty in defining Si-Si bonds in highly disordered SiC, it has been recommended to use the *C* homonuclear bond ratio, χ, which is defined as the ratio of C-C bonds to Si-C bonds. $\chi=0$ describes the com-

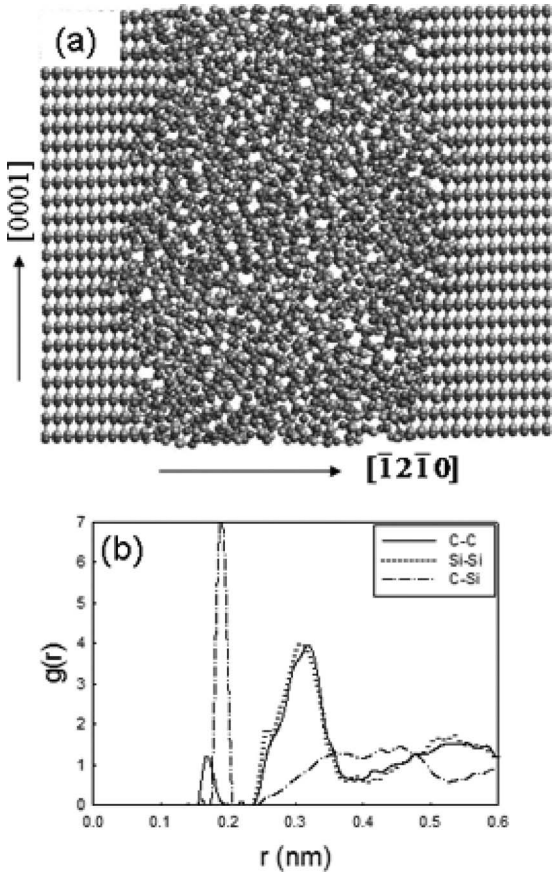

FIG. 1. (a) Atomic plot showing the central part of the crystal, where the melt-quenched amorphous layer lacks any degree of long-range order and two *a-c* interfaces can be clearly seen. Dark spheres indicate Si atoms, while light grey spheres represent C atoms. (b) The C-C, Si-Si, and Si-C pair-correlation functions of the melt-quenched amorphous layer.

pletely ordered state of SiC, whereas $\chi=1$ describes the completely disordered structure of SiC. However, this ratio is sensitive to the choice of bond cutoff distance in *a*-SiC. The cutoff distances of 0.2 and 0.22 nm are used in the present work to calculate C-C bonds and Si-C bonds, respectively, because the C-C and Si-C pair-correlation functions are zero around these values, as shown in Fig. 1(b). The short-range disorder parameter for the melt-quenched region, χ, is 0.14, which is consistent with the value of 0.13 obtained in a melt-quenched bulk SiC.[32]

In order to monitor the recrystallization process of the amorphous layer and the movement of *a-c* interfaces, it is necessary to develop a procedure that allows the identification of the two phases in an effective way. Some work along this direction was proposed by Uttormark *et al.*[33] in the studies of dissolution of crystalline silicon embryos in a liquid phase using MD simulations. They used three different criteria to identify the atoms belonging to the crystalline phase, one of them based on the coordination of the atoms and the other two on the angle distributions. As pointed out by Marqués *et al.*,[16] these criteria are not sufficient to identify an amorphous structure, since the amorphous state has short-range order and shares some of the structural features of the

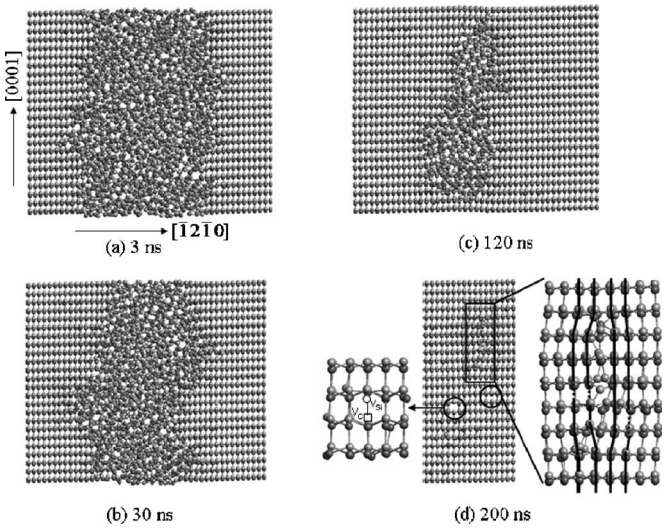

FIG. 2. The recrystallization process in the model M_x, as defined in the text, as a function of time, where atom representation is the same as in Fig. 1. Two circles in (d) indicate the divacancy clusters formed at the end of annealing simulation, and one of the divacancy clusters is enlarged on the left of the plot, where the white sphere represents the Si vacancy and white square the C vacancy. Also, a small region containing an interstitial loop is enlarged on the right of the plot, where the dashed lines sketched reveal the character of the interstitial loop.

crystalline phase. Marqués *et al.*[16] developed a procedure to identify crystalline and amorphous atoms by taking the time average of the atomic positions for several hundred simulation time steps. In addition to the determining the coordination of atoms, as suggested by Uttormark *et al.*,[33] the three-body correlation function for a perfect crystal is also calculated by averaging the atomic positions for the same time at the same temperature. Then, two sets of calculations are compared to identify crystalline and amorphous atoms. A similar approach has been employed in the present study. The time for averaging atomic positions is about two picoseconds, which is enough to obtain accurate averaged configurations to discriminate between crystalline and amorphous atoms. If a Si or a C atom is fourfold coordinated with its neighbors (C or Si atoms) and the six possible angles between the corresponding bonds fall within the limits of the averaged distribution for a perfect crystal at the same temperature, the atom is considered to be crystalline. Conversely, if this condition is not fulfilled, the atom is denoted as part of an amorphous network.

Results of annealing simulations at 1500 K are shown in Fig. 2 as a function of time, the recrystallized state after 3 ns in Fig. 2(a), after 30 ns in Fig. 2(b), after 120 ns in Fig. 2(c) and after 200 ns in Fig. 2(d). The atomic projections are viewed perpendicular to the interfaces on the *xz* plane, where the *X* and *Z* axes are oriented along the $[\bar{1}2\bar{1}0]$ and [0001] crystallographic directions, respectively. The amorphous-crystalline interfaces and their movement in time are demonstrated very clearly in Fig. 2, and the interface positions may be followed from plots of the planar density of atoms as a function of distance along the $[\bar{1}2\bar{1}0]$ direction. However, the

images plotted in Fig. 2 indicate that the recrystallization is not completely planar, and the crystalline portion increases with increasing time. In SPEG, the mobility of atoms is very low, and the process is probably related to local atomic relaxations that overcome dangling bonds and bond defects at the interfaces, rather than long-range thermal or atomic transport. The detailed analysis of atomic configurations (as well as mean-squared displacements) reveals that the C atoms undergo short distance diffusion, while the Si atoms simply rearrange around the C atoms. This indicates that the C atoms near the interfaces play an important role in recrystallization. The complete recrystallization of the M_x model is achieved in about 200 ns at 1500 K.

It can be seen that some defects remain at the center of the simulation cell after recrystallization, as indicated by the circles in Fig. 2(d), and these defects consist of divacancy clusters (V_{Si}-V_C). Also, a small interstitial loop is formed at the end of the simulation, and the region containing this loop is enlarged on the right of Fig. 2(d), which shows more clearly the atomic configurations. The interstitials form an extra plane, as indicated by a solid line, with a stacking fault along the [0001] direction. Because the core structure of the interstitial loop is highly distorted, it is difficult to determine its Burgers vector. Similar microstructures are observed in the simulated anneals at 2000 K. Annealing simulations at 1000 K were carried out for about 260 ns, but complete recrystallization is not observed at 1000 K over the present achievable simulation times. The present results are in good agreement with experimental observations on postirradiation annealing of damage accumulation in 4*H*-SiC,[10] and recrystallization of implantation-induced amorphous region along the $[\bar{1}2\bar{1}0]$ direction in 4*H*-SiC (Ref. 34) and 6*H*-SiC.[35] Zhang *et al.*[10] studied the effects of implantation temperature and ion flux on damage accumulation under Al ion irradiation in 4*H*-SiC, and the amorphous sample was annealed at a temperature of 450 K. The results suggest that planar defects are generated through the agglomeration of excess Si and C interstitials during postirradiation annealing, and some vacancy clusters are also observed. Solid phase epitaxy of implantation-induced amorphous layer in $(\bar{1}2\bar{1}0)$-oriented 6*H*-SiC (Ref. 35) indicates that regrowth layer at 1023 K is recrystallized to the 6*H* polytype, and residual defects extend from the surface to the original *a*-*c* interface.

IV. ANNEALING THE M_y MODEL

As described above, the amorphous region has been prepared using a melt-quenching approach, which extends along the $[\bar{1}010]$ direction. Results of annealing simulations at 2000 K are plotted in Fig. 3 as a function of time, where atomic projections are viewed perpendicular to the interfaces on the *yz* plane. In this case, the *Y* and *Z* axes are oriented along the $[0\bar{1}10]$ and [0001] crystallographic directions, respectively. The epitaxial regrowth of a crystalline state at the interfaces and the movement of the interfaces are generally similar to those observed in the M_x model. The recrystallization takes place continuously, and the crystalline portion increases with increasing time. The recrystallized SiC grows

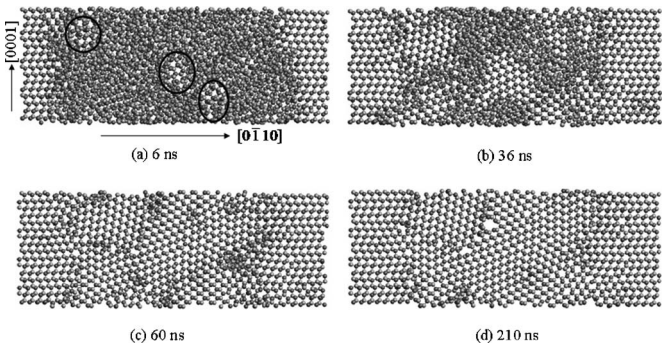

FIG. 3. The recrystallization process in the model M_y as a function of time, where atom representation is the same as in Fig. 1. The nucleation and growth of the secondary ordered phases at the interfaces and inside the amorphous region can be clearly seen.

epitaxially from the original amorphous and/or crystalline interface, and it has an identical crystallographic direction to the substrate.

In addition to the SPEG process at the interfaces, one of the interesting observations from the present simulations is that secondary ordered phases nucleate and grow within the amorphous region, as shown in Fig. 3. During the annealing simulations, three distinct nucleation sites can be seen in Fig. 3(a) within the circles, and these nucleation sites serve as the seeds for the growth of the secondary ordered phases. Two crystalline sites are nucleated inside the amorphous region, while another appears near the interface. After a time of 36 ns, two small crystalline regions are well defined, as shown in Fig. 3(b), and the fraction of crystalline atoms inside the amorphous region increases with increasing time. In addition, the microcrystals can grow into a larger crystalline region by a coarsening process, where the secondary ordered phase forms a continuous network embedded in the perfect 4*H*-SiC. Complete recrystallization is reached after about 210 ns at 2000 K. However, it is clear that the formation of secondary ordered phase at the interfaces hinders the SPEG process in 4*H*-SiC, which may suggest that much higher temperatures are required to completely recover the 4*H* structure along the $[0\bar{1}10]$ crystallographic direction than the $[\bar{1}2\bar{1}0]$ direction. This has been observed experimentally by Satoh *et al.*[35] in 6*H*-SiC, where the regrowth rate of implantation-induced amorphous layer is faster for $(\bar{1}2\bar{1}0)$-orientated sample than that for $(0\bar{1}10)$-orientated sample, or a higher temperature is needed for $(0\bar{1}10)$-orientated sample to achieve the same regrowth rate. In comparison with the annealing simulations of the M_x model (Fig. 2), the dynamic recrystallization processes from small spherical seeds in the M_y model is much slower, which may be related to the interface geometry. The *a*-*c* transition is more difficult from a spherical seed than from a planar interface because the number of bonds available for crystallization at the seed surface is lower. This indicates that a higher value for the activation energy is needed. Once the microcrystal is large enough for its surface to be considered planar on the atomic scale, the dynamic growth processes should be similar to those of the planar interface. The final structure of the recrystallized state is shown in Fig. 3(d). The

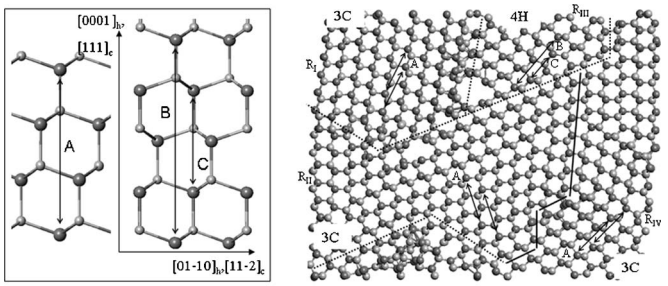

FIG. 4. (a) Lattice structure of 3*C*- and 4*H*-SiC, where crystal axes are given in hexagonal and cubic notation. The lattice can be constructed by a two-dimensional periodic arrangement of the intersection of Si-C dimer rows with the basal plane, where the rows are perpendicular to this plane, While only one type of dimer rows (A) exists in 3*C*-SiC, there are two rows (B and C) in 4*H*-SiC. (b) Atomic structure at the center region of the crystal shown in Fig. 2(d), where the arrows represent the atomic rows defined in (a), and the dashed lines and solid lines indicate the interfaces between different microcrystals and stacking faults formed during the simulations.

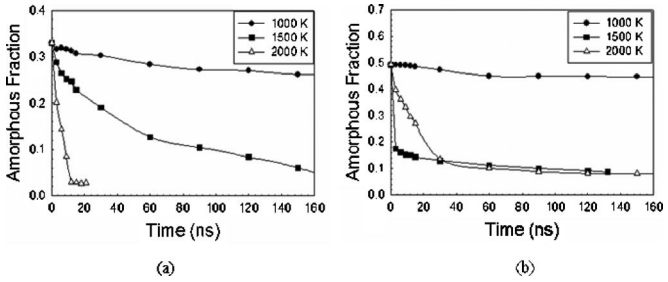

FIG. 5. Variation of amorphous fractions as a function of simulation time at different temperatures for (a) the model M_x and (b) the model M_y.

atoms at the grain boundaries are partially ordered, and a large number of dangling bonds are formed. The transition regions between different grains consist of a few atomic layers. These structures have been annealed for times up to about 300 ns, but complete transformation of these polycrystalline phases to the original 4*H*-SiC is not observed.

In order to understand the structures of the secondary ordered phases, a local region at the central part of the crystal in Fig. 3(d) is shown in Fig. 4, together with the perfectly stacked layers of CSi_4 (or SiC_4) tetrahedra in 3*C*- and 4*H*-SiC to support the interpretation of the present work. As previously noted,[36] in addition to stacking sequences along the *c* axis, different SiC polytypes can be characterized using the dimer rows that are perpendicular to the basal plane. Figure 4(a) illustrates the stacked layers of CSi_4 (or SiC_4) tetrahedra and the different dimer rows in 3*C*- and 4*H*-SiC. The lattice can be established by a two-dimensional periodic arrangement of the intersections of these dimer rows with the basal plane. In 3*C*-SiC, only one type of dimer row, called row *A*, exists, which means the number of nonequivalent Si and C sites is one. In 4*H*-SiC, there are two different rows, namely rows *B* and *C*, which leads to two nonequivalent sites for both Si and C. The sites on rows *B* and *C* are often called hexagonal and cubic sites, respectively.[37] It has been suggested that this notation is not sufficient, because the sites on row *C* in 4*H*-SiC and the sites on row *A* in 3*C*-SiC have identical first and second nearest neighbors, but their third neighbor shells are different. Therefore, the sites on row *C* are not completely equivalent to those in the cubic polytype. The microstructure of recrystallized region is rather complicated, and there exist four distinct crystalline domains that are denoted as R_I, R_{II}, R_{III}, and R_{IV} in Fig. 4(b). Most of these domains, such as R_I, R_{II}, and R_{III}, can be identified as 3*C*-SiC microcrystals. For example, the atoms in R_I consist of only row *A*, as indicated in Fig. 4(b). These microcrystal domains have different crystallographic orientations. Some of these domains are separated by grains boundaries, which consist of transition regions, as indicated by dotted lines. However, it should be noted that bond mismatches exist at the interfaces between R_{II} and R_{IV} domains, and the transition from one domain to another is rather smooth. These mismatches result in the formation of a number of stacking faults, which are shown by solid lines in Fig. 4(b). The microcrystal domain, R_{III}, has a 4*H*-SiC structure because there are two different atomic rows, similar to the *B* and *C* rows shown in Fig. 4(a), but their orientation is different from that of the original 4*H*-SiC.

V. RECRYSTALLIZATION ALONG THE [0$\bar{1}$10] DIRECTION VS THE [$\bar{1}$2$\bar{1}$0] DIRECTION

The number of perfect and amorphous atoms is determined as a function of time using the method described above, and the amorphous fraction, defined as a ratio of amorphous atoms to the total number of atoms, is calculated. The change in amorphous fraction is shown in Figs. 5(a) and 5(b) for the models M_x and M_y, respectively. These results, together with the annealing simulations shown in Figs. 2 and 3, suggest that, at each annealing temperature, the recrystallization progresses through several distinct recrystallization stages as time advances. During the first few nanoseconds of the annealing process, there is a very rapid decrease in the amorphous fraction that is followed by one or more additional distinct recrystallization stages. The rapid recrystallization of implantation-induced amorphous region has been observed experimentally in 4*H*-SiC,[34] which is partially attributed to rapid annealing of the isolated amorphous clusters. The present MD simulations show that the initial recovery stage is characterized by the annihilation or relaxation of point and bond-type defects at the interfaces, which leads to an initially very rapid solid-phase epitaxial growth. While annealing at 1000 K was carried out for much longer times (up to 250 ns), no significant additional recrystallization is observed beyond 60 ns. It is interesting to see that the rapid decrease in the amorphous fraction at 1500 K is much faster than that at 2000 K in the M_y model. As has been noted, only epitaxial recrystallization at the interfaces occurs at 1500 K in this model, whereas the nucleation of secondary ordered phases at the interfaces and inside the amorphous region occurs at earlier stages at 2000 K. These secondary phases grow into large ordered microcrystals. Further epitaxial regrowth is impeded by the nucleation and grain growth of

these secondary phases, which leads to a slower reduction of amorphous fraction at 2000 K. However, the behavior of amorphous fraction at 2000 K in the M_x model is different from that in the M_y model, with a much faster recovery rate, which is consistent with experimental observations in 6*H*-SiC.[35] The nucleation of secondary ordered phases in the M_x model is also observed, but appears only after significant recrystallization has occurred, where the size of the amorphous region is much smaller than that of the original amorphous region. On the other hand, the nucleation of secondary ordered phases in the M_y model appears at a very early stage, where the size of the amorphous region is similar to that of the original amorphous region. The small amorphous region may decrease the growth probability of secondary phases because the number of amorphous atoms that can transfer to crystalline nuclei is small. However, the secondary ordered nuclei in the M_x model disappear during the simulations, just before complete recrystallization. This may suggest that the size of the amorphous region has a significant effect on the growth of the secondary ordered nuclei, rather than on nucleation.

Rutherford backscattering spectrometry in conjunction with channeling, positron annihilation spectroscopy and cross-sectional transmission electron microscopy (TEM) techniques has been employed to study annealing behavior of amorphous SiC layers.[10,12,14,34,35,38] Most of the recrystallization studies have been carried out in 6*H*-SiC (Refs. 10, 12, 14, and 38) along $\langle 0001 \rangle$ direction. Although the stacking sequences along $\langle 0001 \rangle$ direction in 6*H*- and 4*H*-SiC are different, they are very similar along $\langle \bar{1}2\bar{1}0 \rangle$ and $\langle 0\bar{1}10 \rangle$ directions. All the results show that the recrystallized layer generally contains a large number of secondary defects and various polytype crystals, such as 3*C*-SiC. This may be attributed to the lack of the atomic stacking sequence of the polystructure at the *a*-*c* interfaces. On the other hand, recrystallization studies along $(\bar{1}2\bar{1}0)$ and $(0\bar{1}10)$-orientated samples in 4*H* (Ref. 34) and 6*H*-SiC (Ref. 25) have shown that the implantation-induced amorphous layer epitaxially regrows to the original polytype structure with secondary defects that are temperature dependent. Although no secondary phase formation is observed experimentally along the $[0\bar{1}10]$ direction during recrystallization,[34] the slower regrowth rate along the $[0\bar{1}10]$ direction, as compared with the $[\bar{1}2\bar{1}0]$ direction, may be correlated to the atomic density of the atomic planes or the formation of secondary ordered polycrystalline during the recrystallization along the $[0\bar{1}10]$ direction, as discussed above. The $[\bar{1}2\bar{1}0]$ direction is the most packed direction for atoms in the basal plane, and the distance between Si (or C) atoms is 0.33 nm, which is smaller than the value of 0.56 nm along the $[0\bar{1}10]$ direction. However, the distance between two Si (or C) atoms on atomic rows *B* and *C* along the [0001] direction [see Fig. 4(a)] is about 1.06 nm and 0.53 nm, respectively. From Fig. 4(a), it is also clear that two Si (or C) atoms on both rows *B* and *C* are separated by a C (or Si) atom, which suggests that the atomic stacking sequence is not as pronounced as that along the $[\bar{1}2\bar{1}0]$ and $[0\bar{1}10]$ directions. Although it is difficult to conduct a full comparison of the present results with those along the [0001] direction, it is expected that the regrowth rate along the $[\bar{1}2\bar{1}0]$ and $[0\bar{1}10]$ directions should be faster than that along the [0001] direction.

Heera *et al.*[39] studied the microstructure of ion-beam-induced recrystallization of amorphous layers on single-crystalline 6*H*-SiC substrates using cross-sectional transmission electron microscopy, and they found that ion irradiation substantially reduces the onset temperature of both the epitaxial layer regrowth and the random nucleation of crystalline grains. Two recrystallization regions have been observed: 6*H*-SiC epitaxially aligned with the underlying substrate and polycrystalline material of random oriented SiC grains of mainly the 3*C*-polytype. One of the interesting issues is why the epitaxial regrowth front breaks into columns. They speculated that either additional atoms introduced by ion implantation or crystalline nuclei formed during irradiation have lead to columnar growth. Harada *et al.*[14] characterized the microstructures of recrystallized layers in Si ion implanted 6*H*-SiC by means of transmission electron microscopy, and the columnar growth of 6*H*-SiC and epitaxial growth of 3*C*-SiC grains were also observed. Their observations, along with TRIM (Transported Range of Ions in Matter) calculations, suggested that the peak depth of the implanted ion distribution does not fit the columnar growth region and also the number density of implanted Si ions at the peak depth is much smaller than the atomic density in *a*-SiC. These results have implied that the columnar growth of 6*H*-SiC is not due to implanted excess Si ions but due to the stacking failure observed in layered 6*H*-SiC. The present simulation results demonstrate that other polytype SiC can nucleate directly within the amorphous region produced in 4*H*-SiC and undergo further growth during annealing. These results are consistent with the experimental observations conducted by Harada *et al.*;[14] additional atoms introduced by ion implantation are not required for a columnar growth of polycrystalline SiC.

VI. ACTIVATION ENERGY SPECTRUM

The annealing simulation results indicate that there exist several recrystallization processes in 4*H*-SiC as a function of time at each temperature. According to annealing theory,[40,41] the recovery or annealing associated with a single independent process over time, t, at temperature, T, is proportional to $\exp[-\nu t \exp(-E/kT)]$, where ν is a characteristic atomic jump frequency, E is the activation energy for the annealing process, and k is the Boltzmann constant. While the recovery stages are not as distinct as those previously observed for annealing simulations in 3*C*-SiC,[20] the data in Fig. 5 demonstrate the annealing associated with several processes over time at different temperatures. As a first-order approximation, the data at each temperature in Fig. 5 are fit to an isothermal recrystallization model for sequential independent annealing processes of the form:

$$f_a = \sum \exp[-\nu_i t \exp(-E_i/kT)], \quad (1)$$

where f_a is the fraction of amorphous atoms, as defined above, and ν_i and E_i are the characteristic jump frequencies

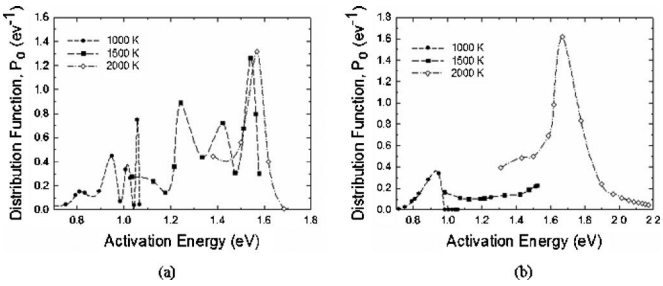

FIG. 6. Activation energy spectra calculated from a model developed for recrystallization processes of (a) the model M_x and (b) the model M_y in 4*H*-SiC, where the time at each annealing temperature samples different regions of activation energy (time-temperature) space according to Eq. (3) in the text.

and activation energies, respectively, for the *i*th recrystallization process. Unfortunately, the data in Fig. 5 are insufficient to yield unique activation energies based on this fitting approach.

A more useful approach, as demonstrated previously for annealing simulations in 3*C*-SiC,[20] is based on annealing theory for a distribution of quasicontinuous independent processes that are characterized by a distribution of jump frequencies and activation energies.[40] The activation energy distribution function, $P_o(E_o)$, for change in f_a is given by the expression[40]

$$P_o(E_o) = -(t/kT)(df_a/dt), \tag{2}$$

where df_a/dt is the rate of change in the amorphous fraction and E_o is the most probable activation energy for annealing to occur for a specific time, temperature, and characteristic jump frequency. The expression for E_o is given by[40]

$$E_o = kT \ln(\nu t). \tag{3}$$

For a single annealing process with a distribution of activation energies or jump frequencies, the activation energy distribution should exhibit a broad peak; in contrast, a process with a very specific activation energy and jump frequency should exhibit a sharp peak in the distribution at the characteristic activation energy for that process, which should be similar to that determined by other methods of analysis.

To apply this method of analysis to the data, the characteristic jump frequency needs to be known or estimated. In the case of SiC, recent MD simulations of close-pair recombination in SiC indicate that the value of ν ranges from 3×10^{12} to 5×10^{14} s^{-1}.[25] Random-walk diffusion processes should have somewhat lower values of ν. Since most recrystallization processes will involve a combination of local relaxation and local diffusion processes, an average value of $\nu = 10^{12}$ s^{-1} is assumed for simplicity. Using this value of ν and by differentiating the simulation data in Fig. 5, a segment of the activation energy distribution given by Eq. (2) is obtained for activation energies defined by Eq. (3) for each time-temperature data set. The results are shown in Figs. 6(a) and 6(b) for the M_x and M_y models, respectively. The different activation energy distributions in Fig. 6(a) overlap to yield a nearly continuous spectrum of activation energies for the various recrystallization processes active over this range of time and temperature. In the case of the M_y model in Fig. 6(b), there are fewer activation energy peaks and less overlap. This may be associated with the difference in dominant recrystallization processes in the M_y model, as discussed above. The initial rapid recrystallization in Figs. 5(a) and 5(b) is associated with short-range defect relaxation processes that are only resolved in the 1000 K distribution and have activation energies of about 0.8 and 1.1 eV, which are similar to activation energies for recombination of some close pairs[26] and for *C* interstitial migration in SiC.[27]

In the M_x model, the rapid recrystallization observed at short times at 2000 K, with activation energies below 1.3 eV is not resolvable on the simulation time scales employed at this temperature. The major recrystallization process observed at 1500 K for longer times and at 2000 K for times longer than a few nanoseconds has an unique activation energy peak at about 1.6 eV, as shown in Fig. 6(a). The highest activation energy values (1.6 eV for the M_x model and 1.7 eV for the M_y model) for full recrystallization processes are somewhat consistent with the experimental value of 2.1 ± 0.5 eV reported for 6*H*-SiC.[42] However, a much higher value of 3.4 eV has been reported for 6*H*-SiC under other crystallographic orientations.[35] This clearly indicates that the different atomic stacking sequence at the *a*-*c* interfaces may have significant effects on the recrystallization mechanisms.

VII. INTERNAL ENERGY DISTRIBUTION

The total potential energy for a system can be calculated by summarizing *N* individual single atomic energies,

$$U = \sum_{i=1}^{N} E_i, \tag{4}$$

where E_i is a single atomic energy of the *i* atom. The single atomic energy can be directly calculated during the MD simulations, and can be used to map out the energy distribution with large spatial resolution that is particularly interesting in the boundary regions between amorphous and crystalline phases. This can also provide interesting features in the grain boundaries between polycrystalline phases formed during simulations. It is noted that the total internal energy can be obtained by summing the total potential energy and the kinetic energy for the ensemble of atoms in the system. Several calculations of the total internal energy at 1500 K in the M_x model indicate small fluctuations, but provide no significant new information. Several frames at different times have been quenched to zero K to see if the energy profiles are significantly different from those at 1500 K, but there are no obvious changes in the energy distribution. These results demonstrate that the total internal energy can be well represented using the total potential energy. The MD cell is divided along $[\bar{1}2\bar{1}0]$ and $[\bar{1}010]$ directions into 30 and 40 layers, with each layer being 0.42 and 0.55 nm for the M_x and M_y models, respectively. The potential energy per atom, defined as the total potential energy divided by the number of atoms in each layer, is plotted in Fig. 7 as a function of distance for the M_x model at 1500 K and the M_y model at 2000 K, where the times inserted in the figures correspond to

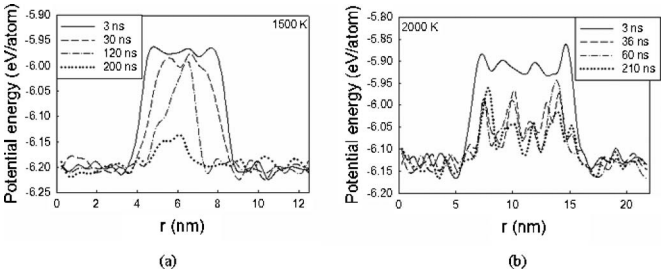

FIG. 7. Energy profiles at different times for (a) the model M_x at 1500 K and (b) the model M_y at 2000 K, where the SPEG processes can be clearly seen by following changes in the width of the energy profiles. The small energy barriers formed at the center of crystal in the model M_y indicate the nucleation and growth of the secondary ordered phases.

those in Figs. 2 and 3. The interfaces between the amorphous and crystalline phases are quite jagged, particularly during the recrystallization processes. The potential energy obtained in the present work may be underestimated, because the layers at the interfaces may include both amorphous and crystalline atoms. However, this does not affect the general conclusions presented below.

At the initial stage, as indicated by solid lines, both plots show energy peaks or barriers appearing at the interfaces, as compared with the adjacent bulk phases. Although the energy barriers are small, this suggests that the atoms at the interfaces are in unfavorable energy configurations. The potential energy of both the crystalline and the amorphous phases away from the interfaces is almost constant, with small fluctuations, and close to the energy of the respective bulk phases. In the M_x model, the width of the energy profiles continuously decreases with increasing simulation time, as shown in Fig. 7(a), which corresponds to the epitaxial recrystallization of the amorphous layer at the interfaces. One of interesting results is that the original barriers at the interfaces disappear after 30 ns annealing at 1500 K, and two new energy peaks are formed, which may be associated with the formation of new *a*-*c* interfaces. On the right of the energy profile at 30 ns, the curve shows a small plateau in the energy, and this may reflect the fact that the exact position of the *a*-*c* interface is no longer well defined, as shown in Fig. 2, where the interface has a zigzag feature. At 120 ns, the energy barrier on the left of the profile vanishes, with only a maximum remaining at the center of the profile. This is consistent with the atomic plot shown in Fig. 2(c), where a small fraction of amorphous atoms exists at the center of the simulation cell. After another 20 ns annealing, the maximum of the energy profile reduces significantly, and the amorphous structure is removed. In the case of the M_y model annealed at 2000 K, the initial energy profile is similar to that in the M_x model; however, the annealing simulations lead to different energy paths. In addition to epitaxial recrystallization of the amorphous layers, as demonstrated by the reduction in the width of the profile, the decrease in the energy level in the original amorphous region is obvious at 36 ns. This is due to the nucleation of polycrystalline phases, as seen in Fig. 3(b). However, there are a few peaks in the energy profile that correspond to the formation of grain boundaries between differently oriented microcrystals. These results imply that atoms in the boundary regions have unfavorable configurations, and thus high energy. The growth of polycrystalline phases further reduces the height of the peaks, but their positions remain unchanged. However, two peaks on the left of the energy profile at 36 ns merge into a single peak as the simulation time advances. The coalescence of the small microcrystals on the left of Fig. 3(b) into a large polycrystalline phase may account for this observation. Although the grain boundaries are not planar along the $\langle \bar{1}010 \rangle$ direction, the internal energy profiles provide the general features of epitaxial recrystallization, as well as the nucleation and growth of the polycrystalline phases. From a comparison of the energy profiles in Fig. 7, it should be noted that the thickness of the amorphous region in the M_y model is larger than that in the M_x model (10 nm vs 4 nm), which may have some effects on the growth of secondary phases, as discussed in the Sec. V. It is also possible that the stronger modulation of the potential energy of the $[0\bar{1}10]$ oriented amorphous layer give rise to the crystallization of secondary ordered phase. However, further investigations are necessary to clarify this issue by simulating recrystallization processes with different sizes of amorphous regions.

VIII. SUMMARY

The recrystallization of nanosized amorphous layers in 4*H*-SiC has been investigated by classical MD methods with simulation times of up to a few hundreds ns at temperatures ranging from 1000 to 2000 K. In general, the recrystallization process is consistent with solid-phase epitaxial regrowth, but the recrystallization mechanism consists of multiple stages. There exist a large number of bond defects at the amorphous-crystalline interfaces, and the recovery of these bond defects and rearrangement of atoms at the interfaces play an important role in recrystallization. The amorphous layer with the *a*-*c* interface normal along $[\bar{1}2\bar{1}0]$ direction can be completely recrystallized at temperatures of 1500 and 2000 K, but the recrystallized region contains defects and interstitial dislocation loops. The temperatures required for complete recrystallization are in good agreement with those observed at experiments. In the model with the *a*-*c* interface normal along $[\bar{1}010]$ direction, the secondary ordered phases nucleate and grow at the interfaces and within the amorphous layer at 2000 K, which hinders the SPEG process. These secondary ordered phases have been identified as 4*H*- and 3*C*-SiC with different crystallographic orientations to the original 4*H*-SiC. The bond mismatches at the interfaces between different microcrystals result in the formation of a number of stacking faults. The temperature is an important parameter to control the nucleation of secondary ordered phase, whereas the size of amorphous region has a significant effect on their growth.

The activation energy spectra for recrystallization along the two directions have been determined. In general, the activation spectra show that there are a number of activation energy peaks associated with different recrystallization processes. The activation energy values for full recrystallization

range from 1.2 to 1.7 eV, and the highest activation energy of 1.7 eV is consistent with the experimental value of 2.1 ± 0.5 eV reported for 6*H*-SiC. The internal energy distribution provides a detailed analysis of energy paths to recrystallization due to SPEG process, and the nucleation and growth of the secondary ordered phases.

ACKNOWLEDGMENT

This research is supported by the Division of Materials Sciences and Engineering, Office of Basic Energy Sciences, U.S. Department of Energy under Contract No. DE-AC05-76RL01830.

*Email address: fei.gao@pnl.gov

[1] W. Bolse, Nucl. Instrum. Methods Phys. Res. B **148**, 83 (1999).
[2] K. Minato, K. Sawa, K. Koya, T. Tomita, A. Ishikawa, C. A. Baldwin, W. A. Gabbard, and C. M. Malone, Nucl. Technol. **131**, 36 (2000).
[3] J. A. Lake, R. G. Bennett, and J. F. Kotek, Sci. Am. **286**, 73 (2002).
[4] R. F. Davies, G. Kelner, M. Shur, J. W. Palmour, and J. A. Edmond, Proc. IEEE **79**, 677 (1991).
[5] A. Hallén, M. S. Janson, A. Yu. Kuznetsov, D. Åberg, M. K. Linnarsson, B. G. Svensson, P. O. Persson, F. H. C. Carlsson, L. Storasta, J. P. Bergman, S. G. Sridhara, and Y. Zhang, Nucl. Instrum. Methods Phys. Res. B **186**, 186 (2002).
[6] L. Malerba and J. M. Perlado, J. Nucl. Mater. **289**, 571 (2001).
[7] Y. Zhang, F. Gao, W. Jiang, D. E. McCready, and W. J. Weber, Phys. Rev. B **70**, 125203 (2004).
[8] M. Ishimaru, I.-T. Bae, and Y. Hirotsu, Phys. Rev. B **68**, 144102 (2003).
[9] F. Gao and W. J. Weber, Phys. Rev. B **66**, 024106 (2002).
[10] Y. Zhang, W. J. Weber, W. Jiang, C. M. Wang, A. Hallén, and G. Possnert, J. Appl. Phys. **93**, 1954 (2003).
[11] J. A. Edmond, S. P. Withrow, H. S. Kong, and R. F. Davis, in *Beam-Solid Interactions and Phase Transformations*, edited by H. Kurz, G. L. Olson, and J. M. Poate, MRS Symposia Proceedings Vol. 51 (Materials Research Society, Pittsburgh, PA, 1986), p. 395–402.
[12] W. Jiang, W. J. Weber, S. Thevuthasan, and D. E. McCready, Nucl. Instrum. Methods Phys. Res. B **143**, 333 (1998).
[13] Y. Zhang, W. J. Weber, W. Jiang, A. Hallén, and G. Possnert, Nucl. Instrum. Methods Phys. Res. B **195**, 320 (2002).
[14] S. Harada, M. Ishimaru, T. Motooka, T. Nakata, T. Yoneda, and M. Inoue, Appl. Phys. Lett. **69**, 3534 (1996).
[15] V. Heera, J. Stoemenos, R. Kögler, and W. Skorupa, J. Appl. Phys. **77**, 2999 (1995).
[16] L. A. Marqués, M. J. Caturla, T. Diaz de la Rubia, and G. H. Gilmer, J. Appl. Phys. **80**, 6160 (1996).
[17] J. K. Bording and J. Taftø, Phys. Rev. B **62**, 8098 (2000).
[18] F. Spaepen and D. Turnbull, in *Laser-Solid Interactions and Laser Processing*, edited by S. D. Ferris, H. J. Leamy, and J. M. Poate (AIP, New York, 1979), p. 73.
[19] N. Bernstein, M. J. Aziz, and E. Kaxiras, Phys. Rev. B **61**, 6696 (2000).
[20] F. Gao, R. Devanathan, Y. Zhang, M. Posselt, and W. J. Weber, J. Mater. Res. **21**, 1420 (2006).
[21] F. Gao, R. Devanathan, Y. Zhang, and W. J. Weber, Nucl. Instrum. Methods Phys. Res. B **228**, 282 (2005).
[22] H. Yano, T. Hirano, T. Kimoto, H. Matsunami, A. Asano, and Y. Sugawara, IEEE Electron Device Lett. **20**, 611 (1999).
[23] F. Gao and W. J. Weber, Nucl. Instrum. Methods Phys. Res. B **191**, 504 (2002).
[24] J. F. Ziegler, J. P. Biersack, and U. Littmark, *The Stopping and Range of Ions in Matter* (Pergamon, New York, 1985).
[25] F. Gao and W. J. Weber, J. Appl. Phys. **94**, 4348 (2003).
[26] M. Bockstedte, A. Mattausch, and O. Pankratov, Phys. Rev. B **69**, 235202 (2004).
[27] F. Gao, W. J. Weber, M. Posselt, and V. Belko, Phys. Rev. B **69**, 245205 (2004).
[28] G. Lucas and L. Pizzagalli, Phys. Rev. B **72**, 161202(R) (2005).
[29] M. Ishimaru, I.-T. Bae, Y. Hirotsu, S. Matsumura, and K. E. Sickafus, Phys. Rev. Lett. **89**, 055502 (2002).
[30] M. Ishimaru, I.-T. Bae, A. Hirata, Y. Hirotsu, J. A. Valdez, and K. E. Sickafus, Nucl. Instrum. Methods Phys. Res. B **242**, 473 (2006).
[31] X. Yuan and L. W. Hobbs, Nucl. Instrum. Methods Phys. Res. B **191**, 74 (2002).
[32] R. Devanathan, F. Gao, and W. J. Weber, Appl. Phys. Lett. **84**, 3909 (2004).
[33] M. J. Uttormark, M. O. Thompson, and P. Clancy, Phys. Rev. B **47**, 15717 (1993).
[34] M. Satoh, T. Hitomi, and T. Suzuki, Nucl. Instrum. Methods Phys. Res. B **242**, 627 (2006).
[35] M. Satoh, Y. Nakaike, and T. Nakamura, J. Appl. Phys. **89**, 1986 (2001).
[36] M. Posselt, F. Gao, W. J. Weber, and V. Belko, J. Phys.: Condens. Matter **16**, 1307 (2004).
[37] P. Pirouz and W. J. Yang, Ultramicroscopy **51**, 189 (1992).
[38] Y. Pacaud, J. Stoemenos, G. Brauer, R. A. Yankov, V. Heera, M. Voelskow, R. Kögler, and W. Skorupa, Nucl. Instrum. Methods Phys. Res. B **120**, 177 (1996).
[39] V. Heera, R. Kögler, W. Skorupa, and J. Stoemenos, Appl. Phys. Lett. **67**, 1999 (1995).
[40] W. Primak, J. Appl. Phys. **31**, 1524 (1960).
[41] A. C. Damak and G. J. Dienes, *Point Defects in Metals* (Gordon and Breach, New York, 1963), Chap. 3, p. 145.
[42] A. Höfgen, V. Heera, F. Eichhorn, W. Skorupa, and W. Möller, Mater. Sci. Eng., B **61–62**, 353 (1999).